



ORIGINAL RESEARCH ARTICLE

Investigation on the Morphology and Formation Mechanism of Porosity in Different Heat Source Regions of Nickel-Based Alloy Laser Hybrid Welding

Yongdu Li, Yang Li, Yuhang Feng, Yuan Zhang, Shuang Li, Xianju zhang, Bin Wang, and Mei Yang 

Submitted: 7 April 2023 / Revised: 20 May 2023 / Accepted: 3 June 2023 / Published online: 16 June 2023

The cross section of the laser-melt inert gas welding (MIG) hybrid welding joint can be divided into two different heat source regions, the upper is the laser-MIG hybrid heat source region, and the lower is the laser heat source region. In this paper, the laser-MIG hybrid welding experiments were carried out on a new nickel-based alloy 4716MA0. The type, morphology and distribution characteristics of porosity in different heat source regions were researched by optical microscopy, scanning electron microscopy and energy-dispersive spectroscopy. In addition, the formation mechanism of different types of stomata was explained by the model diagram. It is found that the dominant region of the laser-MIG hybrid heat source is dominated by metallurgical porosity, which is attributed to the formation of CO gas, whereas the dominant area of the laser heat source is dominated by process porosity. The generation of process porosity is attributed to the instability of the keyhole.

Keywords keyhole, laser-MIG hybrid welding, nickel-based alloy, porosity, welding heat source

1. Introduction

Due to their high strength and excellent corrosion resistance at moderate temperatures, high-temperature nickel-based alloys are widely used in oil drilling, aerospace, nuclear power, and other fields, such as turbine impellers, gas turbine blades, nuclear reactor heat exchangers and light water reactors, and oil and gas well tubular. (Ref 1-7). The Ni element in the alloy forms a solid solution with the residual elements, and a certain amount of the residual elements are consumed, so that the precipitation tendency of harmful phases in the nickel-based alloy can be reduced, and the alloy has excellent mechanical properties (Ref 8, 9). In addition, it contains Cr, Mo, and other elements that can resist various acid corrosion and stress corrosion. Therefore, nickel-based alloys have broad application prospects in the industrial field.

Nickel-based alloys are mostly formed into workpieces suitable for service conditions by welding technology. It is found that there are pores in the weld of the nickel-based alloy under inappropriate fusion welding process, but the porosity

can be reduced by appropriate process parameters (Ref 10-14). The existence of porosity defects seriously restricts the wide application of nickel-based alloys (Ref 15, 16). In particular, the liquid metal in the nickel-based alloy welding pool has poor fluidity due to its high viscosity (Ref 17), which is not conducive to the timely overflow of bubbles in the pool, and it is easy to form welding pores. According to some studies, the main causes of welding pores are active elements, high saturated vapor pressure, and instability of keyhole, and there are generally two types of pores, namely metallurgical pores and process pores (Ref 18-20). It is believed that the main reason for the formation of technological pores is that when the high-energy heat source radiates to the front wall of the keyhole, the front wall of the keyhole is in a state of constant fluctuation, and pits appear on the back wall, and finally, the collapse of the pits induces the generation of bubbles (Ref 21, 22). The formation of metallurgical pores is mainly caused by metallurgical reactions, the change in bath temperature, and the decrease in gas solubility (Ref 23, 24).

Compared with other welding methods, laser welding has the advantages of high-energy density, high welding efficiency, small welding deformation, and good welding integrity (Ref 25-29), and is applied to the welding of nickel-based alloys. Shen et al. (Ref 30) obtained the welded joint of nickel NiTi-20Zr high-temperature shape memory alloy with an excellent performance by laser welding. Oliveira et al. (Ref 31) obtained a joint of Ni-rich NiTiHf high-temperature shape memory alloy with excellent properties by laser welding. To obtain more stable welding joints, in recent years, the welding technology of nickel-based alloys has experienced from arc welding with a single heat source to laser welding with a single heat source (Ref 32, 33). At the same time, there are also reports about the porosity of nickel-based alloy arc welding and laser welding. Kuo et al. (Ref 34) studied the porosity in laser welding of Inconel690 nickel-based alloy, and the results showed that the generation of porosity was

Yongdu Li, Yuhang Feng, Shuang Li, Xianju zhang, and Bin Wang, School of New Energy and Materials, Southwest Petroleum University, Chengdu, China; **Yang Li and Yuan Zhang**, Sichuan Petroleum Construction Co. Ltd, Chengdu, China; and **Mei Yang**, School of New Energy and Materials, Southwest Petroleum University, Chengdu, China; and Sichuan Provincial Engineering Research Center of Advanced Materials Manufacturing Technology for Shale Gas High-Efficient Exploitation, Chengdu, China. Contact e-mail: 380056676@qq.com.

Table 1 Chemical composition of in nickel-based alloy 4716MA0 (mass fraction wt.%)

C	Cr	Co	W	Mo	Al	Ti	Ta	B	Zr	Hf	Ni
0.15	8.2	10	10	0.7	5.5	1.04	2.9	0.13	0.027	1.26	Bal.

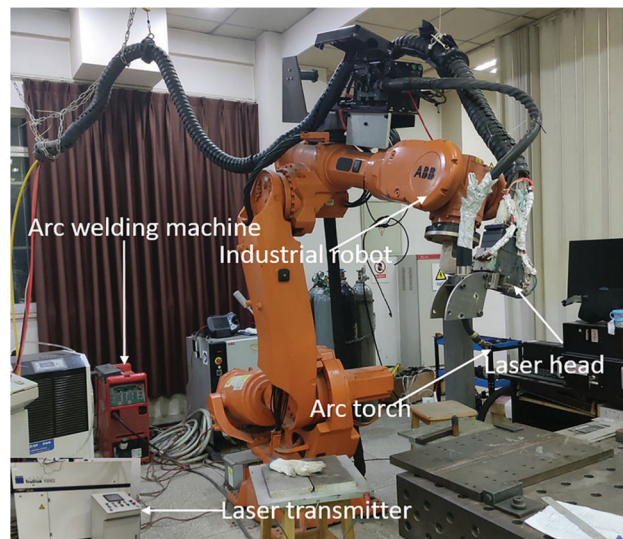
Table 2 Chemical composition of welding wire (mass fraction wt.%)

C	Si	Mn	P	S	Ni	Mo	Cu	Cr	Nb + Ti	Fe
0.013	0.03	0.02	0.001	0.001	65.0	8.85	0.001	21.9	3.65	0.16

related to the fluidity of molten pool metal, and the number of weld porosity could be reduced by adjusting the key process parameters such as laser power. According to the research of Zhao et al. (Ref 35), the welding pores of TIG welding with a single heat source are mainly keyhole-type process pores with irregular shapes. Yu's (Ref 36) research found that under single heat source pulsed laser welding, spherical CO metallurgical pores were dominant, and the formation of the gas was mainly caused by the interaction of C and O elements in the atmosphere and base metal, and then the gas was locked in the weld by the solidified molten pool; in single heat source continuous laser welding, the irregular keyhole process porosity is dominant, which is caused by the collapse of the keyhole, and the keyhole cannot exist stably in the welding process. It is also believed that the metallurgical pores of nickel-based alloy welding are mainly H₂O pores, and there are also H₂ and CO pores (Ref 37, 38).

To overcome the high porosity rate of single heat source arc welding and laser welding, laser-MIG hybrid welding technology has attracted the attention of many researchers at home and abroad. Compared with the traditional single heat source welding technology, laser-MIG hybrid welding combines laser and arc, which have completely different physical properties and energy transfer mechanisms, and acts on the welding position of the material together, which can not only give full play to the advantages of the two heat sources at the same time, but also greatly avoid its shortcomings (Ref 39, 40). Laser-MIG hybrid welding technology can effectively reduce the welding porosity in the welding of aluminum alloy (Ref 41, 42). Unfortunately, there are few reports on the study of pores in laser-MIG hybrid welding of nickel-based alloys. Therefore, it is of great significance to study the porosity in laser-MIG welding of nickel-based alloys.

In this paper, two joint specimens under the optimal welding process (the joint efficiency is 93.7%) were selected, and the morphology and distribution of pores in different heat source regions of the two specimens were observed and analyzed. In addition, the formation mechanism of the pores in the two regions was analyzed based on the morphology and distribution of the pores. The main purpose of this paper is to study the characteristics of pores in different heat source zones of laser-MIG hybrid welding of nickel-based alloy 4716MA0, reveal the formation mechanism of pores, and provide theoretical and experimental basis for the practical application of laser-MIG hybrid welding technology of nickel-based alloy 4716MA0.

**Fig. 1** Laser-arc compound welding systems

2. Experiment Details

2.1 Materials and Equipment

The experiments were carried out using a new nickel-based alloy 4716MA0 developed by an enterprise, the chemical composition of which is shown in Table 1. The design dimensions of the weld base material are 100 × 100 × 3 mm. ERNiCrMo-3 wire with a diameter of 1.2 mm was used for the filler experiments and its chemical composition is shown in Table 2.

A laser-arc hybrid welding system is used in the experiment, and the main body of the system is an arc-laser hybrid robot arm. The welding heat source is the laser (YLS-4000-S2T-CL) and the arc welding equipment (Kemp Arc Pulse 450), and the equipment diagram is shown in Fig. 1.

2.2 Experiment Methods

Before this experiment, the cutting surface of the metal plate was polished, and then, the surface of the plate was cleaned with acetone solution.

Laser-MIG hybrid welding uses the coaxial hybrid mode of the laser beam in the front and arc in the back. The schematic diagram of the welding process is shown in Fig. 2. Pure Ar is

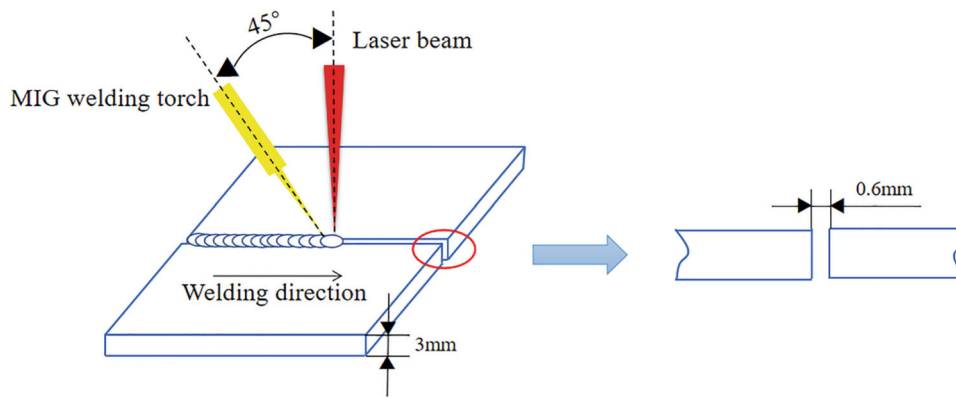


Fig. 2 Schematic diagram of the laser-MIG compound welding process

Table 3 Process parameters of laser-MIG hybrid welding

Number	Laser power, W	Wire feed speed, mm/s	Welding speed, mm/s	MIG welding current, A	MIG welding voltage, V
1	1800	6.5	15	159	26
2	2300	6.5	15	165	26.5
3	2800	6.5	15	165	27.2

Table 4 Tensile strength data of welded joints under different laser power

Laser power, W	Tensile strength, MPa	Average value, MPa	Joint efficiency
1800	876.6, 890.3, 899.8	888.9	91.6%
2300	915.5, 910.4, 903.5	909.8	93.7%
2800	896.9, 902.4, 914.5	904.6	93.2%

used as the shielding gas and the flow rate is 11 L/min. The focal spot diameter is 250 μm , the fiber laser wavelength is 1.06 μm , and the heat source distance (the horizontal distance between the laser action point and the electrode tip) is 3 mm. Considering that the weld should not collapse due to excessive welding energy and that the welding beam should penetrate the weld completely, the samples were welded with the parameters shown in Table 3.

After welding, the tensile properties of welded joints under different laser powers were tested according to G/BT 2651-2008 Tensile Test Method for Welded Joints. The tensile strength of base metal is 970.0 MPa. From the tensile test data in Table 4, the tensile strength of the joint is the highest at 2300 W.

Based on the tensile test, two joint samples were randomly selected under the laser power of 2300 W. The metallographic preparation and detection are carried out according to GB/T14999.4-94 High-Temperature Alloy Microstructure Test Method. After cutting, grinding, and polishing, the samples were etched (12 V DC, 10 s) by an MS-1502DS electrolytic etching instrument with 5% nitric acid methanol solution. The porosity distribution and morphology of the weld were observed by DME-300 M metallographic microscope. The

microstructure of the porosity was observed by the ZEISS EV0 MA15 scanning electron microscope, and the elements in the pores were analyzed by EDS.

3. Results

3.1 Morphology of Porosity in Laser-MIG Hybrid Heat Source Region

The porosity morphology in the laser-MIG hybrid heat source dominant region is shown in Fig. 3 and 4. The porosities of 1# and 2# specimens are distributed in the center of the weld, the shape is a regular circle, and the diameter is about 65 and 25 μm . Ordered grain morphology can be seen in the porosity wall, and there is also second phase precipitation, which can be judged as typical metallurgical porosity from the morphology. The external shape of the metallurgical porosity and the orderliness of the grains in the pore wall suggest that the liquid metal around such porosity is solidified in a more stable state. The crack existence was found in the hole, the formation of which can seriously reduce the mechanical properties of the welded joint and be a source of crack expansion during tension.

Table 5 shows the statistics of EDS results in metallurgical porosity. EDS testing of their porosity walls revealed that the elemental content of C, O, and Si within the porosity of both specimens was higher than that of the corresponding weld metal, and the elemental content of Ni was lower compared to both. It can be inferred that composite oxides of C, Si, and Ni are generated within the porosity in the region dominated by the laser-MIG composite heat source. Compared to specimen 2#, which has a higher O and Si content in the porosity, the second phase precipitated in its porosity is probably a mixture of metal oxides and intermetallic compounds of elements such as Si. Due to many C and O elements gathered in the hole, it can be presumed that the nickel-based alloy laser-MIG welding metallurgical porosity to CO porosity dominated. The formation of CO is mainly since more O may be dissolved in the liquid metal at high temperature, and O is easy to oxidize with Ni at high temperature to form NiO, which can react with C in the liquid metal to form CO. The source of a large amount of C and O may mainly come from the involvement of the atmosphere, which is difficult to completely prevent even with the protection of argon.

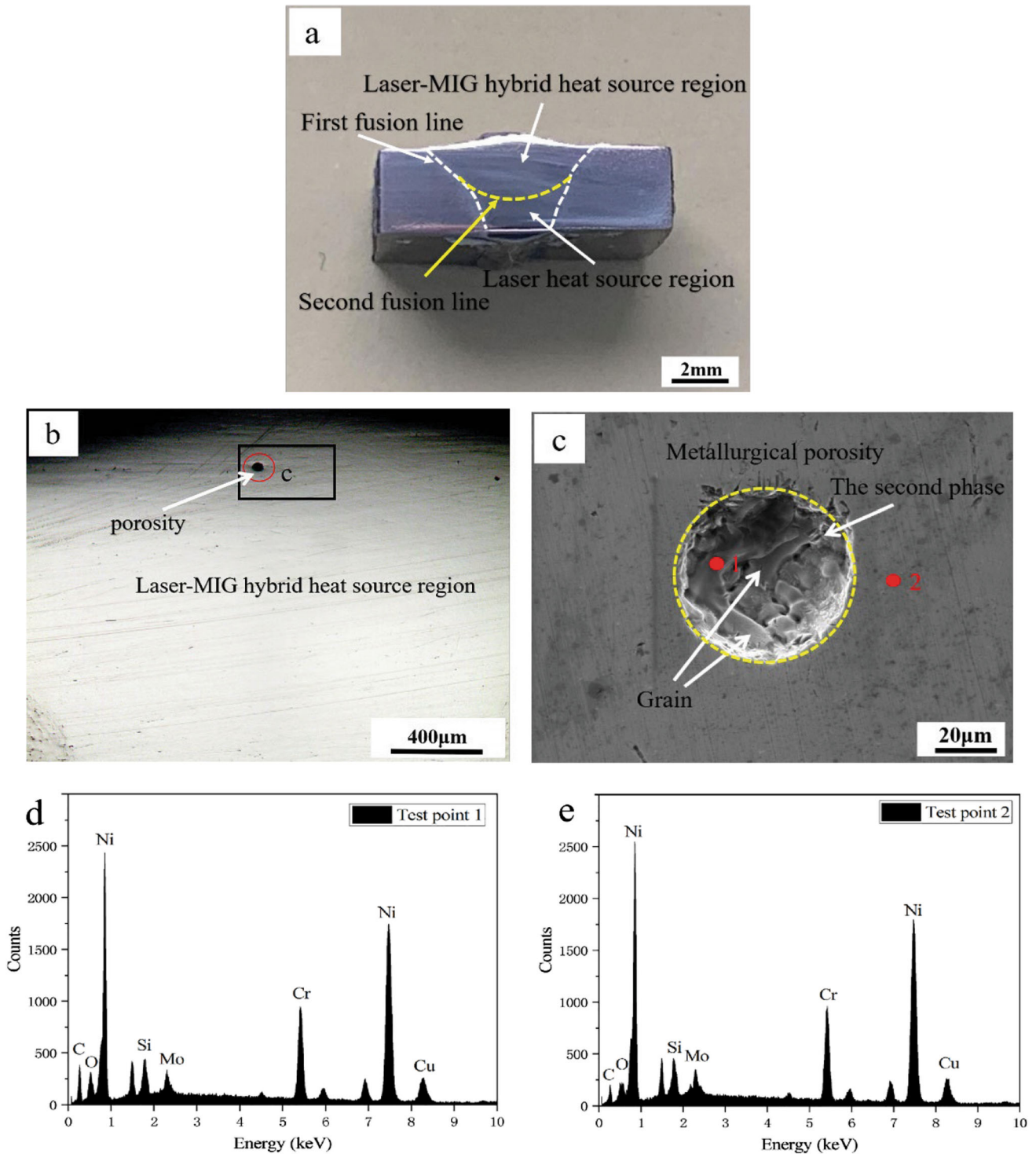


Fig. 3 1# Specimen porosity morphology and elemental analysis: (a) regional distribution of dominant heat sources; (b), (c) porosity morphology map; (d), (e) porosity EDS result

3.2 Morphology of Porosity in Laser Heat Source Region

The porosity morphology in the laser heat source dominated area is shown in Fig. 5 and 6. The pores on 1 # and 2 # samples are mainly distributed in the inner side of the first fusion line of the weld, and their shape and size are irregular. There are particles attached to the porosity wall, and the grain morphol-

ogy can be seen faintly. There are also cracks in the pores, which can be judged as typical process porosity from morphology. From the external shape of the process porosity and the irregularity of the grains on the pore walls, it can be shown that the liquid metal around such pores solidifies in a more violent state (Ref 43). The attached particles may be because the fusion zone is close to the base metal, the

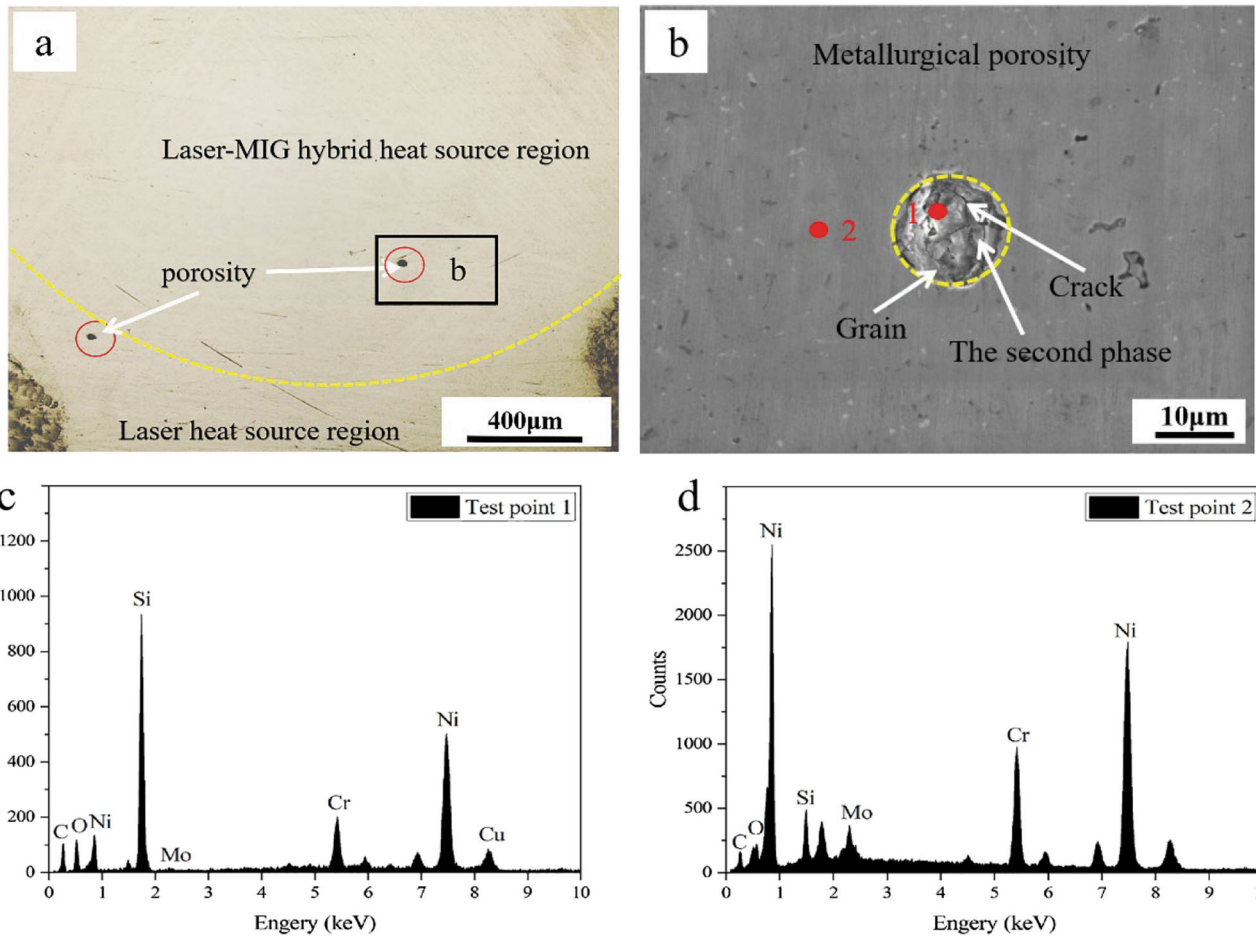


Fig. 4 2# Specimen porosity morphology and elemental analysis: (a), (b) porosity morphology map; (c), (d) porosity EDS results

Table 5 The EDS result in the inner wall of metallurgy porosity (mass fraction wt.%)

Specimen	Test site	C	O	Si	Ni
1#	1	15.32	2.16	0.75	63.18
	2	8.56	0.42	0.66	69.55
2#	1	16.50	4.67	16.68	50.94
	2	7.72	0.13	0.75	70.03

temperature is relatively low, and there are some unmelted solid particles in the fusion zone. The unmelted solid particles reduce the working section of the welded joint to a certain extent and affect the mechanical properties of the weld. During the solidification of the weld, the unmelted fine particles adhere to the inner wall of the pore. From Fig. 5(b), it can be observed that there are many caterpillar-like small pores around the large pores, and local small pores merge with the large pores. This is mainly because the pressure of the newly formed small worm-like bubble is lower than that of the large bubble. Driven by the flow and pressure of the molten pool, the small bubble moves closer to the large bubble and eventually merges with the large hole.

Table 6 shows the statistics of EDS results in process porosity. Compared with the weld metal, the contents of C, O,

and Si in the holes of the two samples increased significantly by EDS. The content of the Ni element is decreased. It can be inferred that a large number of oxides such as C, Si, and Ni may also be formed in the pores. Judging from the irregular shape of the pores, the formation process of the CO process pores is as follows: when CO gas is generated at the bottom of the weld at a high temperature, the CO gas is rolled into a pit formed by the collapse of an unstable keyhole, and then the pit, which is sealed by molten metal and separated separately, makes it difficult for the CO gas to overflow, thus forming process pores with irregular shapes. It is worth noting that the content of C and O detected on the hole wall is significantly higher than that of the metallurgical pore arm, which may be because when the laser beam penetrates the whole weld, there is no argon protection on the back of the weld, and a large amount of air is involved in the weld.

4. Discussion

4.1 Force Analysis of Gas Bubbles in Laser-MIG Hybrid Welding

Melting to solidification of the laser-MIG welded joint is a very complex dynamic process. Inside the molten pool, the liquid metal flows downward at both ends of the keyhole under the combined action of the acting force of the keyhole on the

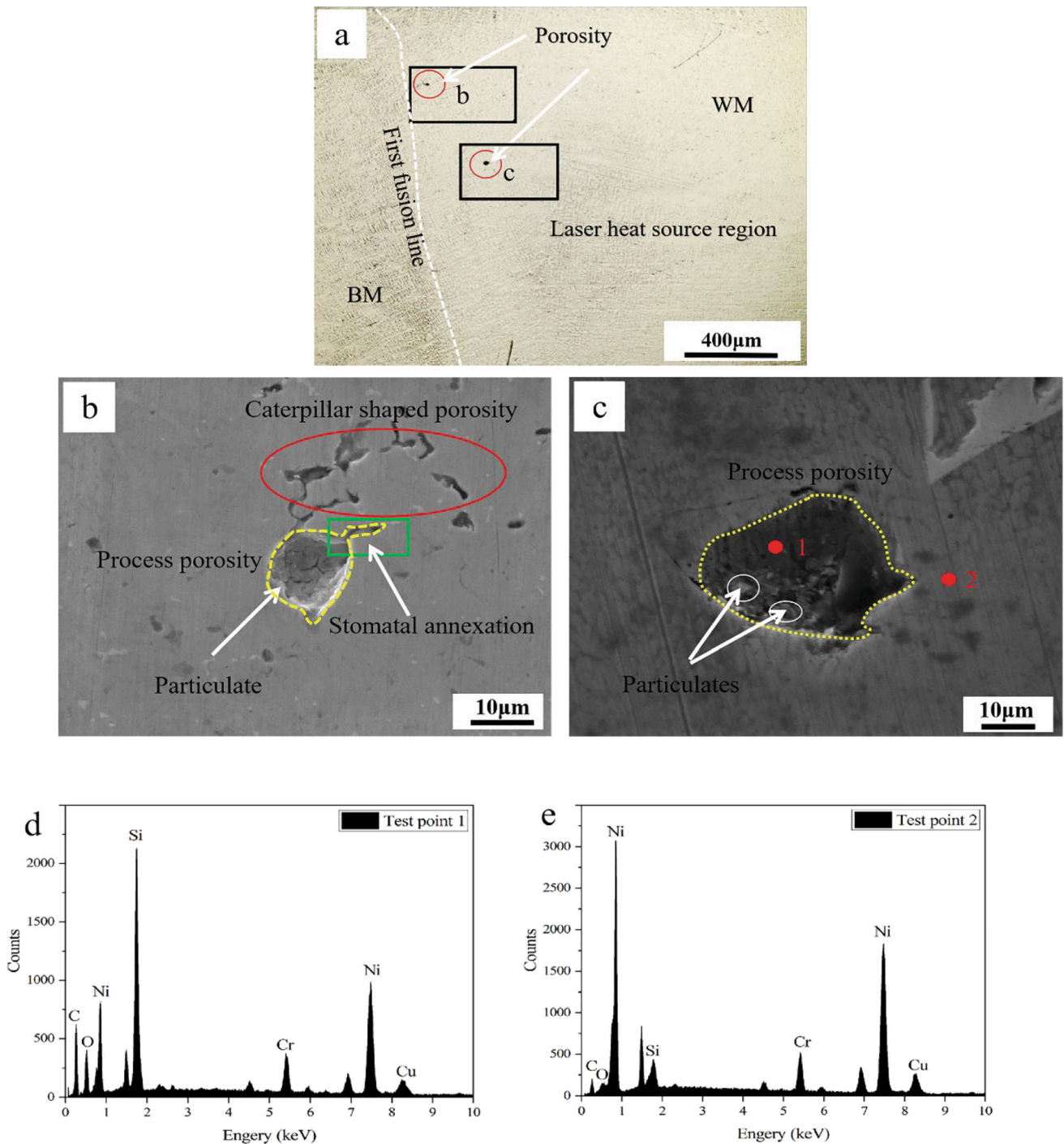


Fig. 5 1# Specimen porosity morphology and elemental analysis: (a) distribution map of porosity; (b), (c) porosity morphology map; (d), (e) porosity EDS results

molten pool, the reaction force of the solid–liquid interface on the molten bath, surface tension, arc force, droplet gravity, and other factors, and begins to flow reversely along the solid–liquid interface after reaching the bottom of the molten bath, as shown in Fig. 7.

Bubble in liquid is mainly subject to bubble gravity (F_g), bubble buoyancy (F), the viscous force of liquid nickel-based alloy (F_d) and thrust force of liquid nickel-based alloy flow (F_t). The thrust force (F_t) caused by the flow of the molten pool

and the buoyancy force (F) of the bubble itself promote the floating of the bubble. However, the gravity of the bubble itself (F_g) and the viscous force of the liquid nickel-based alloy (F_d) hinder the floating and escape of the bubble.

4.2 Formation Mechanism of Process Porosity in Laser-MIG Hybrid Welding

The formation mechanism of porosities in the laser-MIG hybrid welding process of nickel-based alloy 4716 MA0 is

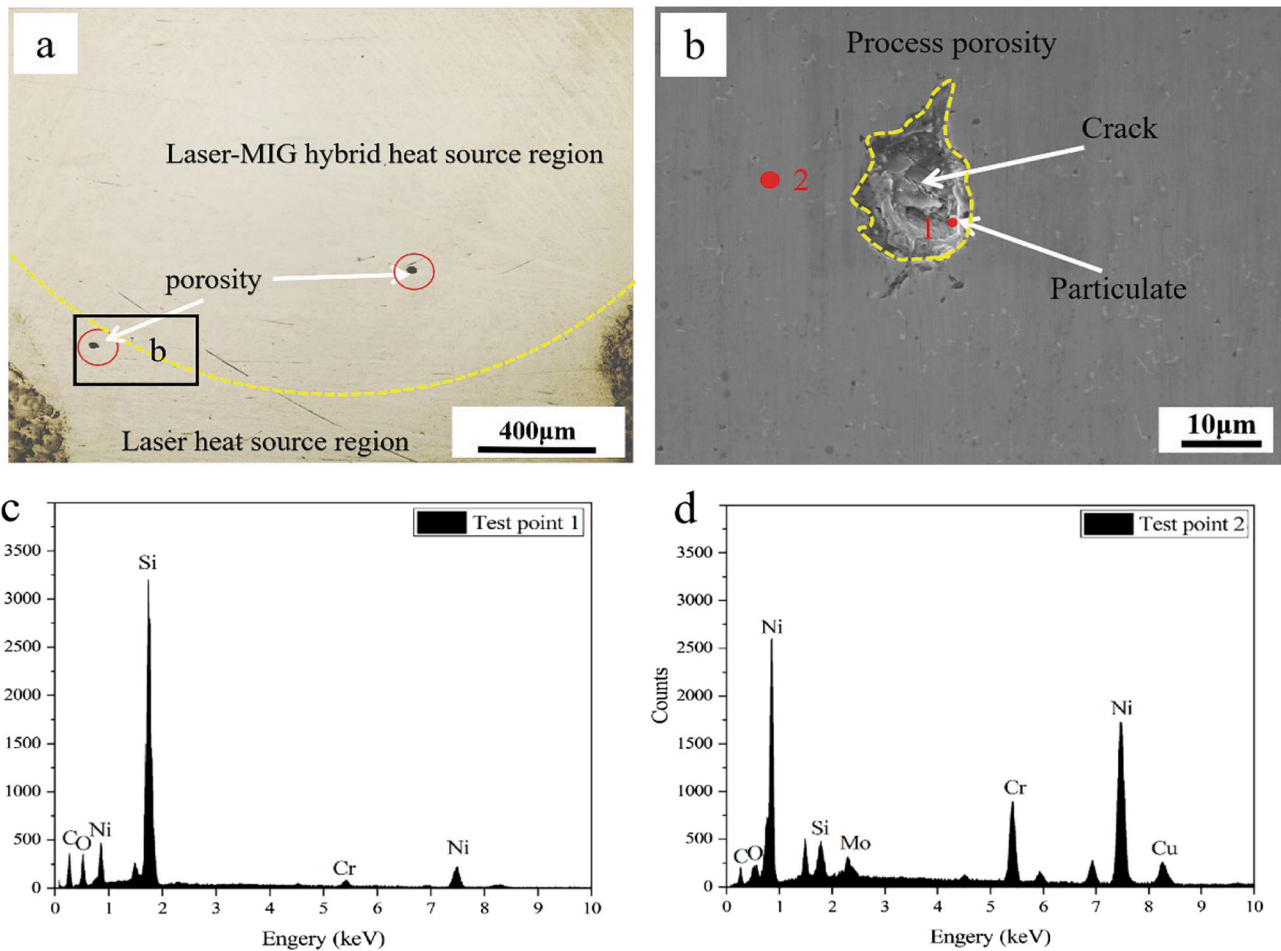


Fig. 6 2# Specimen porosity morphology and elemental analysis: (a) distribution map of porosity; (b) porosity morphology map; (c), (d) porosity EDS results

Table 6 The EDS result in the inner wall of process porosity (mass fraction wt.%)

Specimen	Test site	C	O	Si	Ni
1#	1	31.34	7.62	12.99	38.71
	2	10.25	0.36	0.46	78.85
2#	1	30.54	8.73	48.61	8.97
	2	9.47	0.44	0.92	69.57

shown in Fig. 8. In the process of laser-MIG hybrid welding of nickel-based alloy 4716 MA0, the surface of the substrate was melted after being irradiated by a high-energy laser beam, and the metal vapor was produced with the continuous action of the laser beam. A penetrating keyhole is formed under the continuous induction of the reaction force of the metal vapor. The strong evaporation of metal vapor leads to the instability of the keyhole, and a pit appears on the back wall of the keyhole. When the pit moves to the bottom of the keyhole, the liquid metal will collapse under the action of gravity (Ref 21). Finally, the pit, which is closed by the molten metal and separated separately, forms a process bubble with an irregular shape. The bubble formed at the bottom of the keyhole moves to the liquid pool with the flow of the liquid metal. In addition, the impact of

the gravity of the MIG filling droplet can also lead to the instability of the keyhole, which is also related to the transfer mode associated with MIG (Ref 44, 45). Thereby further promoting the formation of process-type bubbles. Because the width of the bottom of the weld is small, the solidification speed of the bottom molten pool is fast. If the bubbles do not float up and overflow in time before the liquid metal solidifies, process porosities will be formed in the bottom of the weld. Therefore, in the lower part of the welding joint, that is, the area where the laser heat source acts, the process porosities are generated.

From Fig. 5(b), there are a large number of small worm-like porosities around the process-type large porosity and that some of the small porosities have merged with the large porosity. The unstable keyhole induced the formation of bubbles of varying sizes. These bubbles move in different directions and at different speeds as they are wrapped in liquid metal. As the internal pressure of the small bubble is lower than that of the large bubble, when the two bubbles with different internal pressures move to a suitable distance, they are driven by a combination of pressure and liquid metal flow, so the two bubbles merge. The merging mechanism of process-type porosity goes through three stages as shown in Fig. 9: the initial separated state, the aggregated state, and the final merged state. For the instability of the laser welding keyhole, Zhang et al. (Ref 46) found that when the laser power decreases, the

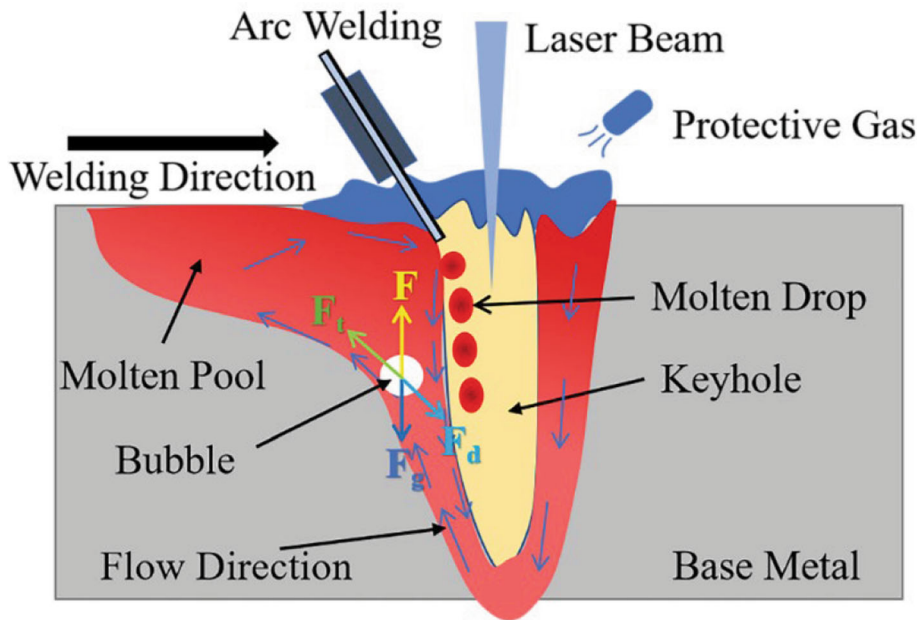


Fig. 7 Bubble stress distribution in molten pool of laser-MIG hybrid welding

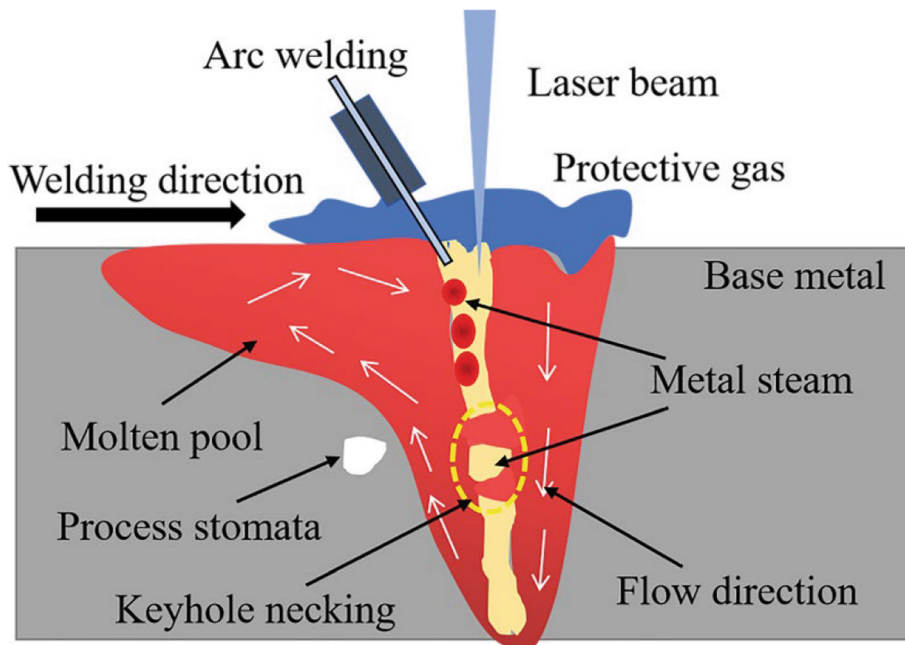


Fig. 8 Porosity formation mechanism in laser-MIG hybrid welding

keyhole depth/width ratio increases, and the keyhole stability will improve. According to Li's research (Ref 47), the swinging laser heat source can improve the stability of the keyhole.

4.3 Formation Mechanism of Metallurgical Porosity in Laser-MIG Hybrid Welding

The above EDS elemental analysis shows that the metallurgical porosity in the laser-MIG hybrid welding of nickel-based alloy 4716 MA0 is mainly caused by CO generated at high temperatures. The O atoms mainly come from the entrapment

of the atmosphere and the H₂O attached to the weldment and the welding rod. In the welding process, even in the atmosphere of inert shielding gas Ar, the O element in the air will be involved in the welding. Therefore, the weldment and welding rod shall be dried before welding, and proper shielding gas flow shall be ensured.

In laser-MIG welding, the O atoms in H₂O are dissociated under the combined high temperature of the laser beam and MIG arc heat. At high temperatures, Ni reacts with O decomposed from H₂O and O entrapped from the atmosphere. Then, the oxide of Ni is reduced by C originally contained in

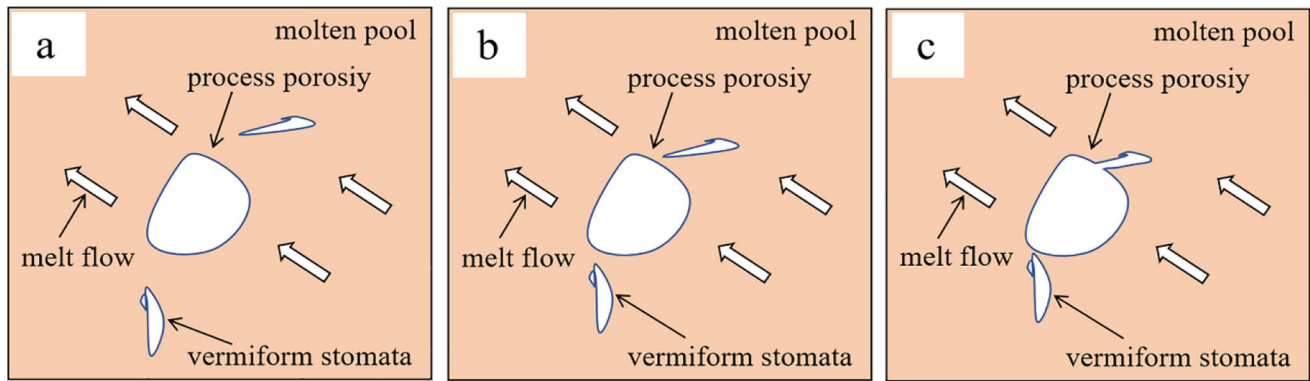


Fig. 9 Keyhole-type stomatal consolidation mechanism: (a) initial separation state; (b) aggregation state; (c) final consolidation state

the nickel-based alloy at high temperature, and finally, CO gas is generated. When the generated CO gas is difficult to dissolve in or react with the liquid nickel-based alloy, it will be stranded in the molten pool before it can escape from the molten pool before solidification and eventually form metallurgical CO pores in the weld. CO porosities are mainly distributed in the upper part of the weld, that is, the laser-MIG hybrid heat source area. This is because the reaction force of metal vapor makes the entrainment of O in the atmosphere mainly concentrated in the upper part of the weld.

5. Conclusion

Nickel-based alloy 4716MA0 laser heat source dominates the area of porosity with process-type porosity. The shape of the pore is irregular, and the pore wall is rough. From the shape of the pores and the characteristics of the inner wall, it can be inferred that the liquid metal around the process pores solidifies in a more intense state. The formation of process porosity is mainly caused by the collapse of the pit at the bottom of the unstable keyhole, so the process porosity appears at the bottom of the weld. In addition, there is a phenomenon of coalescence between process pores.

The pores in the main heat source area of laser-MIG hybrid welding of Ni-based alloy 4716 MA0 are mainly metallurgical. The shape of this kind of pore is regular and the pore wall is relatively smooth. From the shape of the pores and the characteristics of the inner wall, it can be inferred that the liquid metal around the metallurgical pores solidifies in a relatively stable state. The formation of metallurgical porosity is mainly caused by the CO formed by the external intrusion of O and C contained in the weldment itself.

Acknowledgments

This research work was supported by the Natural Science Foundation of Sichuan Province of China(2022NSFSC0325), Application foundation project of Sichuan Science and Technology department (No.2021YJ0346), State Key Laboratory of Long-life High-Temperature Materials (DTCC28EE200795) and Sichuan Provincial Engineering Research Center of Advanced Materials Manufacturing Technology for Shale Gas High-efficient Exploitation(2022SCYYQKCL008).

References

1. M. Azari, E. Rasti, M.H.R. Dehkordi et al., Investigation of Temperature Distribution and Melt Pool Microstructure in Laser Fusion Welding of Inconel 625 Superalloy, *J. Laser Appl.*, 2021, **33**(2), p 022015
2. I. Sah, J.-B. Hwang, W.-G. Kim et al., High-Temperature Mechanical Behaviors of Diffusion-Welded Alloy 617, *Nucl. Eng. Des.*, 2020, **364**, p 110617
3. P.M. Scott and P. Combrade, General Corrosion and Stress Corrosion Cracking of Alloy 600 in Light Water Reactor Primary Coolants, *J. Nucl. Mater.*, 2019, **524**, p 340–375
4. S. Sharma, R.V. Taiwade, and H. Vashishtha, Effect of Pulsed Current Gas Tungsten Arc Process on the Dissimilar Weldments between Nickel-Based Superalloy/Austenitic Stainless Steel, *ISIJ Int.*, 2017, **57**(6), p 1080–1086
5. O. Stanners, J. Russell, S. John et al., Powder Interlayer Bonding of Nickel-Based Superalloys with Dissimilar Chemistries, *Materials*, 2021, **14**(8), p 2029
6. R. Min-Xu, Y. C-L, Z.R.L. X-Q, L. D-P, Effect of Temperature on Corrosion Resistance of Nickel-based Alloy 718 in Highly Acidic Environment. *Mater. Protect.*, 2017, **50**(3), p. 88–90
7. M. Alizadeh-Sh, S.P.H. Marashi, E. Ranjbarbodeh, R. Shoja-Razavi, and J.P. Oliveira, Prediction of Solidification Cracking by an Empirical-Statistical Analysis for Laser Cladding of Inconel 718 Powder on a Non-weldable Substrate, *Opt. Laser Technol.*, 2020, **128**, p 106244
8. A. Chyrkin, W.G. Sloof, R. Pillai et al., Modelling Compositional Changes in Nickel Base Alloy 602 CA during High Temperature Oxidation, *Mater. High Temp.*, 2015, **32**(1–2), p 102–112
9. J. Dong, M. Zhang, X. Xie et al., Interfacial Segregation and Cosegregation Behaviour in a Nickel-Base Alloy 718, *Mater. Sci. Eng. A*, 2002, **328**(1), p 8–13
10. F.C. Neto, M. Pereira, L.E.S. Dos Santos Paes et al., Effect of Power Modulation Frequency on Porosity Formation in Laser Welding of SAE 1020 Steels, *Int. J. Adv. Manuf. Technol.*, 2021, **112**(9), p 2509–17
11. L. Chen, C. Wang, L. Xiong et al., Microstructural, Porosity and Mechanical Properties of Lap Joint Laser Welding for 5182 and 6061 Dissimilar Aluminum Alloys under Different Place Configurations, *Mater. Des.*, 2020, **191**, p 108625
12. W. Tao and S. Yang, Weld Zone Porosity Elimination Process in Remote Laser Welding of AA5182-O Aluminum Alloy Lap-Joints, *J. Mater. Process. Technol.*, 2020, **286**, p 116826
13. X. Xu, G. Song, S. Zhao et al., Effect of Distance between the Heat Sources on Energy Transfer Behavior in Keyhole during Laser-GTA Welding Titanium Alloy, *J. Manuf. Process.*, 2020, **55**, p 317–325
14. X. Zhan, Y. Zhao, Z. Liu et al., Microstructure and Porosity Characteristics of 5A06 Aluminum Alloy Joints Using Laser-MIG Hybrid Welding, *J. Manuf. Process.*, 2018, **35**, p 437–445
15. L.A. James and W.J. Mills, Fatigue-Crack Propagation Behaviour of Defective Weldments, *Int. J. Press. Vessel. Pip.*, 1981, **9**(5), p 367–383
16. W. Jiang, P. Li, W.-X. Yao et al., The Effect of Porosity Size and Oxidation on the HCF Property of Nickel-Based Single Crystal Superalloy at 980 °C, *Theor. Appl. Fract. Mech.*, 2022, **120**, p 103423

17. Y. Zhu, Y. Cai, H. Dong et al., Tailoring Droplet Transfer and Molten Pool Flow during Hybrid Laser Arc Welding of Nickel Base Alloy, *Opt. Laser Technol.*, 2022, **147**, p 107620
18. M. Jiang, X. Chen, Y. Chen et al., Mitigation of Porosity Defects in Fiber Laser Welding under Low Vacuum, *J. Mater. Process. Technol.*, 2020, **276**, p 116385
19. W. Tan, N.S. Bailey, and Y.C. Shin, Investigation of Keyhole Plume and Molten Pool Based on a Three-Dimensional Dynamic Model with Sharp Interface Formulation, *J. Phys. D Appl. Phys.*, 2013, **46**(5), p 055501
20. C. Zhang, Y. Yu, C. Chen et al., Suppressing Porosity of a Laser Keyhole Welded Al-6Mg Alloy via Beam Oscillation, *J. Mater. Process. Technol.*, 2020, **278**, p 116382
21. M. Miyagi, Y. Kawahito, H. Kawakami et al., Dynamics of Solid-Liquid Interface and Porosity Formation Determined Through X-Ray Phase-Contrast in Laser Welding of Pure Al, *J. Mater. Process. Technol.*, 2017, **250**, p 9–15r
22. S. Katayama, Y. Kawahito, and M. Mizutani, Elucidation of Laser Welding Phenomena and Factors Affecting Weld Penetration and Welding Defects, *Phys. Procedia*, 2010, **5**, p 9–17
23. V.I. Ryazantsev and V.A. Fedoseev, Metallurgical and Technological Porosity of Aluminium Alloys in Arc Welding, *Weld. Int.*, 2002, **16**(4), p 320–324
24. Y. Zhao, X. Zhou, T. Liu et al., Investigate on the Porosity Morphology and Formation Mechanism in Laser-MIG Hybrid Welded Joint for 5A06 Aluminum Alloy with Y-Shaped Groove, *J. Manuf. Process.*, 2020, **57**, p 847–56
25. B. Kessler, D. Dittrich, B. Brenner et al., Extension of the Process Limits in Laser Beam Welding of Thick-Walled Components Using the Laser Multi-pass Narrow-Gap welding (Laser-MPNG) on the Example of the Nickel-Based Material Alloy 617 OCC, *Weld. World*, 2021, **65**(7), p 1359–1371
26. I. Tlili, D. Baleanu, S.M. Sajadi et al., Numerical and Experimental Analysis of Temperature Distribution and Melt Flow in Fiber Laser Welding of Inconel 625, *Int. J. Adv. Manuf. Technol.*, 2022, **121**(1), p 765–784
27. D. Wu, B. Cheng, J. Liu et al., Water Cooling Assisted Laser Dissimilar Welding with Filler Wire of Nickel-Based Alloy/Austenitic Stainless Steel, *J. Manuf. Process.*, 2019, **45**, p 652–660
28. S. Zhang, Y. Wang, M. Zhu et al., Effects of Heat Source Arrangements on Laser-MAG Hybrid Welding Characteristics and Defect Formation Mechanism of 10CrNi3MoV Steel, *J. Manuf. Process.*, 2020, **58**, p 563–573
29. H. Xia, L. Li, C. Tan et al., In Situ SEM Study on Tensile Fractured Behavior of Al/Steel Laser Welding-Brazing Interface, *Mater. Des.*, 2022, **224**, p 111320
30. J.P. Oliveira, J. Shen, J.D. Escobar, C.A.F. Salvador, N. Schell, N. Zhou, and O. Benafan, Laser Welding of H-Phase Strengthened Ni-Rich NiTi-20Zr High Temperature Shape Memory Alloy, *Mater. Des.*, 2021, **202**, p 109533
31. J.P. Oliveira, N. Schell, N. Zhou, L. Wood, and O. Benafan, Laser Welding of Precipitation Strengthened Ni-rich NiTiHf High Temperature Shape Memory Alloys: Microstructure and Mechanical Properties, *Mater. Des.*, 2019, **162**, p 229–234
32. W. Pacquentin, L. Gouton, N. Caron et al., Laser Surface Melting of Nickel-Based Alloy Reduces Nickel Release in the Primary Cooling System of a Nuclear Power Plant, *Opt. Laser Technol.*, 2021, **144**, p 107401
33. S. Zhou, G. Ma, W. Dongjiang et al., Ultrasonic Vibration Assisted Laser Welding of Nickel-Based Alloy and Austenite Stainless Steel, *J. Manuf. Process.*, 2018, **31**, p 759–767
34. T.Y. Kuo, Effects of Pulsed and Continuous Nd-YAG Laser Beam Waves on Welding of Inconel Alloy, *Sci. Technol. Weld. Join.*, 2005, **10**(5), p 557–565
35. Z.X.L. Yanhong, Effect of Welding Process on Porosity in Nickel-based Welding Seam, *Nonferrous Met. Mater. Eng.*, 2018, **39**(3), 36–42
36. K. Yu, Study on Microstructure, Property Evolution and Corrosion Behavior of Laser Welded GH3535 Alloy. University of Chinese Academy of Sciences, 2018
37. Z. MIN, J. H-J, Welding of Nickel-based Alloy N06690 Pipe [J]. *Pipeline Tech. Equip.*, 2014, (2), p. 38–40
38. L.I. Sorokin and Z.A. Sidlin, Evaluation of the Effect of Alloying Elements on Pore Formation When Welding Nickel-Chromium Alloys, *Weld. Int.*, 1998, **12**, p 229–232
39. G. Wu, Aluminum Alloy Laser Numerical Analysis of Residual Stress and Deformation in -TIG hybrid welding [J], University of Electronic Science and Technology of China, 2012
40. X. Zhan, Y. Li, W. Ou et al., Comparison between Hybrid Laser-MIG Welding and MIG Welding for the Invar36 Alloy, *Opt. Laser Technol.*, 2016, **85**, p 75–84
41. L. Huang, D. Wu, X. Hua et al., Effect of the Welding Direction on the Microstructural Characterization in Fiber Laser-GMAW Hybrid Welding of 5083 Aluminum Alloy, *J. Manuf. Process.*, 2018, **31**, p 514–522
42. B. Ribic, T.A. Palmer, and T. Debroy, Problems and Issues in Laser-Arc Hybrid Welding, *Int. Mater. Rev.*, 2009, **54**(4), p 223–244
43. Y. Yin, H. Chen, X. Yang et al., Investigation of Porosity in Rotating Laser-MIG Hybrid Welding A6N01 Aluminum Alloy, *Int. J. Mod. Phys. B*, 2018, **33**(01n03), p 1940029
44. J. Shen, R. Gonçalves, Y.T. Choi et al., Microstructure and Mechanical Properties of Gas Metal Arc Welded CoCrFeMnNi Joints Using a 308 Stainless Steel Filler Metal, *Scr. Mater.*, 2023, **222**, p 115053
45. J. Shen, R. Gonçalves, Y.T. Choi et al., Microstructure and Mechanical Properties of Gas Metal Arc Welded CoCrFeMnNi Joints Using a 410 Stainless Steel Filler Metal, *Mater. Sci. Eng. A*, 2022, **857**, p 144025
46. D. Zhang, M. Wang, C. Shu et al., Dynamic Keyhole Behavior and Keyhole Instability in High Power Fiber Laser Welding of Stainless Steel, *Opt. Laser Technol.*, 2019, **114**, p 1–9
47. M. Li, Study on Welding of Titanium Alloy with Wobble Laser Welding and TIG Composite Welding with Filler Wire and the Mechanism of Porosity Suppression [J], Hunan University, 2021

Publisher's Note Springer Nature remains neutral with regard to jurisdictional claims in published maps and institutional affiliations.

Springer Nature or its licensor (e.g. a society or other partner) holds exclusive rights to this article under a publishing agreement with the author(s) or other rightsholder(s); author self-archiving of the accepted manuscript version of this article is solely governed by the terms of such publishing agreement and applicable law.